Noname manuscript No.
(will be inserted by the editor)

A Stable High–Order Perturbation of Surfaces/Asymptotic Waveform Evaluation Method for the Numerical Solution of Grating Scattering Problems

Matthew Kehoe and David P. Nicholls

the date of receipt and acceptance should be inserted later

Abstract The scattering of electromagnetic radiation by a layered periodic diffraction grating is an important model in engineering and the sciences. The numerical simulation of this experiment has been widely explored in the literature and we advocate for a novel interfacial method which is perturbative in nature. More specifically, we extend a recently developed High–Order Perturbation of Surfaces/Asymptotic Waveform Evaluation (HOPS/AWE) algorithm to utilize a stabilized numerical scheme which also suggests a rigorous convergence result. An implementation of this algorithm is described, validated, and utilized in a sequence of challenging and physically relevant numerical experiments.

Keywords: High–Order Perturbation of Surfaces Methods; Asymptotic Waveform Evaluation; High–Order Spectral Methods; Helmholtz equation; Layered Media.

MSC: 65N35, 78A45, 78B22

1 Introduction

The scattering of linear waves by a periodic layered structure is a central model in many problems of scientific and engineering interest. Examples arise in areas such as geophysics [60,5], imaging [41], materials science [24], nanoplasmonics [54,38,23], and oceanography [7]. In the particular case of nanoplasmonics, there are many important topics such as extraordinary optical transmission [22], surface enhanced spectroscopy [39], and surface plasmon resonance (SPR) biosensing [27,40,29,32].

Due to their technological importance, the numerical simulation of these diffraction gratings has generated a huge amount of interest including the

---

Matthew Kehoe and David P. Nicholls
Department of Mathematics, Statistics, and Computer Science,
University of Illinois at Chicago, Chicago, IL 60607
E-mail: davidn@uic.edu

application of all of the classical approaches, e.g., Finite Differences [36], Finite Elements [30], Discontinuous Galerkin [26], Spectral Elements [21], and Spectral Methods [25,6,58]. For general geometries these specify extremely useful and accurate tools (e.g., COMSOL Multiphysics [18]) for engineers and scientists alike. However, for structures with simplifying features, such as homogeneous layering, these can be needlessly expensive due to the unnecessary discretization of layer interiors. To address this, a whole class of *interfacial* methods have been developed of which Boundary Integral/Boundary Element Methods (BIM/BEM) are the most widely used [17,35,57]. These posit unknowns at the layer interfaces thereby reducing the number of degrees of freedom by an order of magnitude. While these schemes require particular care in their implementation (e.g., the design of special quadrature rules to achieve high–order accuracy, sophisticated algorithms to rapidly sum the quasi–periodized Green function, and appropriate preconditioning strategies for the iterative solution of the Non–Symmetric Positive Definite linear system of equations) there are well–known implementations that deliver results of surpassing accuracy and stability, see, e.g., [9–11].

In this paper we focus upon a very particular Quantity of Interest (QoI) in the study of diffraction gratings, the Reflectivity Map, which is representative of a group of performance metrics for which we develop a special class of interfacial numerical algorithms. The Reflectivity Map, R, measures the response (reflected energy) of a periodically corrugated grating structure as a function of illumination frequency, ω, and corrugation amplitude, h. For each of the algorithms listed above, the response at any given (ω, h) pair requires a new simulation restarted from scratch. A High–Order Perturbation of Surfaces (HOPS) method [49,50] takes a perturbative view towards the geometric dependence of R on $h = \varepsilon$ by seeking the terms in the expansion about $\varepsilon = 0$,

$$R = R(\varepsilon) = \sum_{n=0}^{\infty} R_n \varepsilon^n.$$

With this one can realize an enormous savings in computational effort by conducting a new computation only for each choice of ω and simply summing the formula above for any desired value of ε. We point out that we have demonstrated in [48,51], for a closely related problem concerning Laplace's equation, that the domain of analyticity in ε is not merely a small disk centered at the origin in the complex plane, but rather a neighborhood of the *entire* real axis. Therefore, provided one utilizes a suitable method of (numerical) analytic continuation (e.g., Padé approximation [3]), one can simulate configurations with interface deformations of *arbitrary* size (see, e.g., [48,28]). We suspect that the analogous result can be discovered for the Helmholtz equation which is relevant here and we intend to verify this in future work.

Taking this philosophy to its natural conclusion, in [43] we considered $\omega = (1+\delta)\underline{\omega} = \underline{\omega} + \delta\underline{\omega}$ and performed a *joint* expansion of this map about $(\varepsilon =$

$0, \omega = \underline{\omega}$)

$$R = R(\varepsilon, \delta) = \sum_{n=0}^{\infty} \sum_{m=0}^{\infty} R_{n,m} \varepsilon^n \delta^m.$$

It seems that a *single* computation, recovering all of the $R_{n,m}$, should be sufficient to discover the *entire* Reflectivity Map. In fact, as demonstrated by Kirsch [34], the situation is not so simple as these expansions are not valid for all values of (ε, δ) and it was found in [43] that the Rayleigh singularities (often called the Wood anomalies) enforced finite–size domains of convergence in δ. However, the results were so encouraging that we now undertake a more in–depth investigation featuring a new formulation in terms of Dirichlet–Neumann Operators computed via an application of the stable, accurate, and rapid Transformed Field Expansions (TFE) algorithm [50] appropriate for a *joint* perturbation expansion. Not only does this deliver an implementation with greatly enhanced stability properties [50], but it also describes an algorithm that can be rigorously justified to be convergent as we demonstrate in a forthcoming publication [33].

The paper is organized as follows. In Section 2 we summarize the equations which govern the propagation of linear electromagnetic waves in a two–dimensional periodic structure. In Section 2.1 we discuss the Transparent Boundary Conditions we utilize to enforce the outgoing wave conditions rigorously, while in Section 2.2 we define the object of our study, the Reflectivity Map. In Section 3 we restate our governing equations in terms of interfacial quantities via a Non–Overlapping Domain Decomposition phrased in terms of Dirichlet–Neumann Operators (DNOs). We discuss our HOPS/AWE approach in Section 4 and our novel approach to computing the DNOs in Section 5 (supplemented with a discussion of expansions of the surface data in Section 5.1). In Section 6 we present our numerical results with a description of implementation details in Section 6.1, our Fourier–Chebyshev method in Section 6.2, and our use of Padé approximation in Section 6.3. We comment on issues of the bounded domains of analyticity in our expansions in Section 6.4. In Section 6.5 we validate our code with the Method of Manufactured Solutions, while in Section 6.6 we present results of multiple numerical simulations of the Reflectivity Map which we conducted. In Section 6.7 we discuss the superior computational complexity our algorithm enjoys for computing objects like the Reflectivity Map. Concluding remarks are given in Section 7.

2 The Governing Equations

In this paper we consider a y–invariant, doubly layered structure with a periodic interface separating the two materials; see Figure 1. The d–periodic interface shape is specified by the graph of the function $z = g(x)$, $g(x + d) = g(x)$. A dielectric (with refractive index n^u) occupies the domain above the interface

$$S^{(u)} := \{z > g(x)\},$$

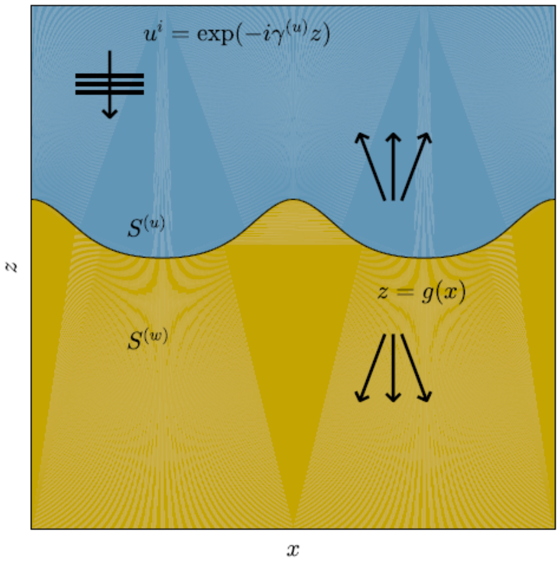

Fig. 1: A two-layer structure with a periodic interface, $z = g(x)$, separating two material layers, $S^{(u)}$ and $S^{(w)}$, illuminated by plane–wave incidence.

while a material of refractive index n^w is in the lower layer

$$S^{(w)} := \{z < g(x)\}.$$

The superscripts are chosen to conform to the notation of the authors in previous work [42,45]. The structure is illuminated from above by monochromatic plane–wave incident radiation of frequency ω and wavenumber $k^u = n^u \omega / c_0 = \omega / c^u$ (c_0 is the speed of light) aligned with the grooves

$$\underline{\mathbf{E}}^i(x, z, t) = \mathbf{A} e^{-i\omega t + i\alpha x - i\gamma^u z}, \quad \underline{\mathbf{H}}^i(x, z, t) = \mathbf{B} e^{-i\omega t + i\alpha x - i\gamma^u z},$$
$$\alpha := k^u \sin(\theta), \quad \gamma^u := k^u \cos(\theta).$$

We consider the reduced incident fields

$$\mathbf{E}^i(x, z) = e^{i\omega t} \underline{\mathbf{E}}^i(x, z, t), \quad \mathbf{H}^i(x, z) = e^{i\omega t} \underline{\mathbf{H}}^i(x, z, t),$$

where the time dependence $\exp(-i\omega t)$ has been factored out. As shown in [52], the reduced electric and magnetic fields $\{\mathbf{E}, \mathbf{H}\}$ are α–quasiperiodic like the incident radiation. To close the problem we specify that the scattered radiation is “outgoing,” upward propagating in $S^{(u)}$ and downward propagating in $S^{(w)}$.

It is well known (see, e.g., Petit [52]) that in this two–dimensional setting, the time–harmonic Maxwell equations decouple into two scalar Helmholtz problems which govern the Transverse Electric (TE) and Transverse Magnetic

(TM) polarizations. We define the invariant (y) direction of the scattered (electric or magnetic) field by $\tilde{u} = \tilde{u}(x,z)$ and $\tilde{w} = \tilde{w}(x,z)$ in $S^{(u)}$ and $S^{(w)}$, respectively. The incident radiation in the upper field is defined as $\tilde{u}^i(x,z)$.

Following our previous work [43] we further factor out the phase $\exp(i\alpha x)$ from the fields $\tilde{u}$ and $\tilde{w}$

$$u(x,z) = e^{-i\alpha x}\tilde{u}(x,z), \quad w(x,z) = e^{-i\alpha x}\tilde{w}(x,z),$$

which, we note, are d–periodic. In light of all of this, we are led to seek outgoing, d-periodic solutions of

$$\Delta u + 2i\alpha\partial_x u + (\gamma^u)^2 u = 0, \qquad z > g(x), \tag{1a}$$
$$\Delta w + 2i\alpha\partial_x w + (\gamma^w)^2 w = 0, \qquad z < g(x), \tag{1b}$$
$$u - w = \zeta, \qquad z = g(x), \tag{1c}$$
$$\partial_N u - i\alpha(\partial_x g)u - \tau^2\left[\partial_N w - i\alpha(\partial_x g)w\right] = \psi, \qquad z = g(x), \tag{1d}$$

where $N := (-\partial_x g, 1)^T$. The Dirichlet and Neumann data are

$$\zeta(x) := -e^{-i\gamma^u g(x)}, \tag{1e}$$
$$\psi(x) := (i\gamma^u + i\alpha(\partial_x g))e^{-i\gamma^u g(x)}, \tag{1f}$$

and

$$\tau^2 = \begin{cases} 1, & \text{TE}, \\ (k^u/k^w)^2 = (n^u/n^w)^2, & \text{TM}, \end{cases}$$

where $k^w = n^w\omega/c_0 = \omega/c^w$ and $\gamma^w = k^w\cos(\theta)$. Due to its importance in the classical study of SPRs we will focus on TM polarization [54].

2.1 Transparent Boundary Conditions

The Upward Propagating Condition (UPC) and Downward Propagating Condition (DPC) [1] rigorously enforce the outgoing wave conditions which we mentioned earlier. We now demonstrate how these can be stated in terms of Transparent Boundary Conditions which also truncate the bi–infinite problem domain to one of finite size. For this we choose values a and b such that

$$a > |g|_{L^\infty}, \quad -b < -|g|_{L^\infty},$$

and define the artificial boundaries $\{z = a\}$ and $\{z = -b\}$. In $\{z > a\}$ the Rayleigh expansions [52] tell us that upward propagating solutions of (1a) are

$$u(x,z) = \sum_{p=-\infty}^{\infty} \hat{a}_p e^{i\tilde{p}x + i\gamma_p^u z}, \tag{2}$$

where, for $p \in \mathbf{Z}$ and $q \in \{u, w\}$,

$$\tilde{p} := \frac{2\pi p}{d}, \quad \alpha_p := \alpha + \tilde{p}, \quad \gamma_p^q := \sqrt{(k^q)^2 - \alpha_p^2}, \quad \mathrm{Im}\left\{\gamma_p^q\right\} \geq 0. \tag{3}$$

In a similar fashion, downward propagating solutions of (1b) in $\{z < -b\}$ can be expressed as

$$w(x,z) = \sum_{p=-\infty}^{\infty} \hat{d}_p e^{i\tilde{p}x - i\gamma_p^w z}.$$

With these we can define the Transparent Boundary Conditions in the following way: Focusing on the UPC (the DPC is similar) we rewrite (2) as

$$u(x,z) = \sum_{p=-\infty}^{\infty} \left(\hat{a}_p e^{i\gamma_p^u a}\right) e^{i\tilde{p}x + i\gamma_p^u (z-a)} = \sum_{p=-\infty}^{\infty} \hat{\xi}_p e^{i\tilde{p}x + i\gamma_p^u (z-a)},$$

and note that,

$$u(x,a) = \sum_{p=-\infty}^{\infty} \hat{\xi}_p e^{i\tilde{p}x} =: \xi(x),$$

and

$$\partial_z u(x,a) = \sum_{p=-\infty}^{\infty} (i\gamma_p^u) \hat{\xi}_p e^{i\tilde{p}x} =: T^u[\xi(x)],$$

which defines the order–one Fourier multiplier T^u. From this we state that upward–propagating solutions of (1a) satisfy the Transparent Boundary Condition at $z = a$

$$\partial_z u(x,a) - T^u[u(x,a)] = 0, \quad z = a. \tag{4}$$

We note that a similar calculation leads to the Transparent Boundary Condition at $z = -b$

$$\partial_z w(x,-b) - T^w[w(x,-b)] = 0, \quad z = -b, \tag{5}$$

where

$$T^w[\psi(x)] := \sum_{p=-\infty}^{\infty} (-i\gamma_p^w) \hat{\psi}_p e^{i\tilde{p}x}.$$

We also point out that solutions which satisfy (4) and (5) equivalently satisfy the UPC and DPC, respectively [1].

With these we now state the full set of governing equations as

$$\begin{aligned}
&\Delta u + 2i\alpha\partial_x u + (\gamma^u)^2 u = 0, && z > g(x), && \text{(6a)}\\
&\Delta w + 2i\alpha\partial_x w + (\gamma^w)^2 w = 0, && z < g(x), && \text{(6b)}\\
&u - w = \zeta, && z = g(x), && \text{(6c)}\\
&\partial_N u - i\alpha(\partial_x g)u - \tau^2 \left[\partial_N w - i\alpha(\partial_x g)w\right] = \psi, && z = g(x), && \text{(6d)}\\
&\partial_z u(x,a) - T^u[u(x,a)] = 0, && z = a, && \text{(6e)}\\
&\partial_z w(x,-b) - T^w[w(x,-b)] = 0, && z = -b, && \text{(6f)}\\
&u(x+d,z) = u(x,z), && && \text{(6g)}\\
&w(x+d,z) = w(x,z). && && \text{(6h)}
\end{aligned}$$

2.2 The Reflectivity Map

Building upon the developments in the previous section we can now define our QoI, the Reflectivity Map. Regarding the solution (2) we note the very different character of the solution for wavenumbers p in the set

$$\mathcal{U}^u := \left\{ p \in \mathbf{Z} \mid \alpha_p^2 < (k^u)^2 \right\},$$

and those that are not. From our choice of the branch of the square root, components of $u(x,z)$ corresponding to $p \in \mathcal{U}^u$ propagate away from the layer interface, while those not in this set decay exponentially from $z = g(x)$. The latter are called evanescent waves while the former are propagating (defining the set of propagating modes $\mathcal{U}^u$) and carry energy away from the grating. With this in mind one defines the efficiencies [52]

$$e_p^u := (\gamma_p^u / \gamma^u) \left| \hat{a}_p \right|^2, \quad p \in \mathcal{U}^u,$$

and the Reflectivity Map

$$R := \sum_{p \in \mathcal{U}^u} e_p^u. \tag{7}$$

Similar quantities can be defined in the lower layer [52], and with these the principle of conservation of energy can be stated for structures composed entirely of dielectrics

$$\sum_{p \in \mathcal{U}^u} e_p^u + \tau^2 \sum_{p \in \mathcal{U}^w} e_p^w = 1.$$

In this situation a useful diagnostic of convergence for a numerical scheme (which we will utilize later) is the "energy defect"

$$D := 1 - \sum_{p \in \mathcal{U}^u} e_p^u - \tau^2 \sum_{p \in \mathcal{U}^w} e_p^w, \tag{8}$$

which should be zero for a purely dielectric structure.

3 A Non–Overlapping Domain Decomposition Method

We now restate our governing equations (6) in terms of *surface* quantities via a Non–Overlapping Domain Decomposition Method [37,20,19]. In particular, if we define

$$\begin{aligned} U(x) &:= u(x, g(x)), \quad & \tilde{U}(x) &:= -\partial_N u(x, g(x)), \\ W(x) &:= w(x, g(x)), \quad & \tilde{W}(x) &:= \partial_N w(x, g(x)), \end{aligned}$$

where u is a d–periodic solution of (6a) and (6e), and w is a d–periodic solution of (6b) and (6f). In terms of these our full governing equations (6) are equivalent to the pair of boundary conditions, (6c) & (6d),

$$U - W = \zeta, \quad -\tilde{U} - (i\alpha)(\partial_x g) U - \tau^2 \left[\tilde{W} - (i\alpha)(\partial_x g) W \right] = \psi.$$

This set of two equations for four unknowns can be closed by noting that the pairs $\{U, \tilde{U}\}$ and $\{W, \tilde{W}\}$ are connected, e.g., by DNOs

$$G : U \to \tilde{U}, \quad J : W \to \tilde{W}.$$

These are well–defined operators for sufficiently smooth g (e.g., $g \in C^2$ [50]) thus we focus on this interfacial reformulation of our governing equations

$$\mathbf{A}\mathbf{V} = \mathbf{R}, \tag{9}$$

where

$$\mathbf{A} = \begin{pmatrix} I & -I \\ G + (\partial_x g)(i\alpha) & \tau^2 J - \tau^2(\partial_x g)(i\alpha) \end{pmatrix}, \quad \mathbf{V} = \begin{pmatrix} U \\ W \end{pmatrix}, \quad \mathbf{R} = \begin{pmatrix} \zeta \\ -\psi \end{pmatrix}. \tag{10}$$

4 A High–Order Perturbation of Surfaces/Asymptotic Waveform Evaluation (HOPS/AWE)

At this point there are many approaches to simulate (9) numerically. We take up a perturbative approach under two assumptions:

1. Boundary Perturbation: $g(x) = \varepsilon f(x)$, $\varepsilon \in \mathbf{R}$,
2. Frequency Perturbation: $\omega = (1+\delta)\underline{\omega} = \underline{\omega} + \delta\underline{\omega}$, $\delta \in \mathbf{R}$.

As we stated in the Introduction, we believe that *real* values of ε which are *arbitrarily* large can be simulated [47,48,51,28] while the values of δ are only limited by the Rayleigh singularities [34,44]. The second assumption has the following important consequences

$$\begin{aligned} k^q &= \omega/c^q = (1+\delta)\underline{\omega}/c^q =: (1+\delta)\underline{k}^q = \underline{k}^q + \delta\underline{k}^q, && q \in \{u, w\}, \\ \alpha &= k^u \sin(\theta) = (1+\delta)\underline{k}^u \sin(\theta) =: (1+\delta)\underline{\alpha} = \underline{\alpha} + \delta\underline{\alpha}, && \\ \gamma^q &= k^q \cos(\theta) = (1+\delta)\underline{k}^q \cos(\theta) =: (1+\delta)\underline{\gamma}^q = \underline{\gamma}^q + \delta\underline{\gamma}^q, && q \in \{u, w\}. \end{aligned}$$

This, in turn, delivers

$$\alpha_p = \alpha + \tilde{p} = \underline{\alpha} + \delta\underline{\alpha} + \tilde{p} =: \underline{\alpha}_p + \delta\underline{\alpha}.$$

At this point we now assume the *joint* analyticity of the operator $\mathbf{A}$ and function $\mathbf{R}$ with respect to ε and δ which will induce a *jointly* analytic solution, $\mathbf{V}$, of (9). (All of this will be rigorously established in a forthcoming publication [33].) In this case we can expand

$$\{\mathbf{A}, \mathbf{V}, \mathbf{R}\}(\varepsilon, \delta) = \sum_{n=0}^{\infty} \sum_{m=0}^{\infty} \{\mathbf{A}_{n,m}, \mathbf{V}_{n,m}, \mathbf{R}_{n,m}\} \varepsilon^n \delta^m, \tag{11}$$

and a straightforward calculation reveals that, at each perturbation order (n,m), we must solve

$$\begin{aligned}\mathbf{A}_{0,0}\mathbf{V}_{n,m} &= \mathbf{R}_{n,m} - \sum_{\ell=0}^{n-1} \mathbf{A}_{n-\ell,0}\mathbf{V}_{\ell,m} - \sum_{r=0}^{m-1} \mathbf{A}_{0,m-r}\mathbf{V}_{n,r} \\ &\quad - \sum_{\ell=0}^{n-1}\sum_{r=0}^{m-1} \mathbf{A}_{n-\ell,m-r}\mathbf{V}_{\ell,r}. \end{aligned} \tag{12}$$

At this point all that remains to be specified are the forms for the $\mathbf{A}_{n,m}$ and $\mathbf{R}_{n,m}$, and a method to invert $\mathbf{A}_{0,0}$.

A brief inspection of the formulas for $\mathbf{A}$ and $\mathbf{R}$, (10), reveals that

$$\mathbf{A}_{0,0} = \begin{pmatrix} I & -I \\ G_{0,0} & \tau^2 J_{0,0} \end{pmatrix}, \tag{13a}$$

$$\begin{aligned}\mathbf{A}_{n,m} &= \begin{pmatrix} 0 & 0 \\ G_{n,m} & \tau^2 J_{n,m} \end{pmatrix} \\ &\quad + \delta_{n,1}\left\{1+\delta_{m,1}\right\}(\partial_x f)(i\underline{\alpha})\begin{pmatrix} 0 & 0 \\ 1 & -\tau^2 \end{pmatrix}, \qquad n \neq 0 \text{ or } m \neq 0, \end{aligned} \tag{13b}$$

$$\mathbf{R}_{n,m} = \begin{pmatrix} \zeta_{n,m} \\ -\psi_{n,m} \end{pmatrix}, \tag{13c}$$

where $\delta_{n,m}$ is the Kronecker delta function. The forms for $\zeta_{n,m}$ and $\psi_{n,m}$, which depend upon the incident radiation (e.g., we will investigate both a non–physical illumination to validate our code, see Section 6.5, and plane–wave incidence, see Section 6.6) can typically be stated explicitly. By contrast, formulas for the (n,m)–th corrections of the Taylor expansions of the DNOs, G and J, must be simulated numerically. For this we advocate the Method of Transformed Field Expansions (TFE) [50] which we review in the following section.

5 Simulation of Dirichlet–Neumann Operators

As we mentioned in the previous section, the only remaining specification for our algorithm is the computation of the (n,m)–th term in the Taylor expansion of the DNOs, G and J. For brevity we restrict our attention to the DNO in the upper layer, $\{g(x) < z < a\}$, and note that the considerations for the lower layer are largely the same.

We recall the precise definition of the upper layer DNO [44]: Given an integer $s \geq 0$ and any $\theta > 0$, if $g \in C^{s+3/2+\theta}$ the unique d–periodic solution of

$$\Delta u + 2i\alpha\partial_x u + (\gamma^u)^2 u = 0, \qquad g(x) < z < a, \tag{14a}$$

$$u(x,g(x)) = U(x), \qquad z = g(x), \tag{14b}$$

$$\partial_z u(x,a) - T^u[u(x,a)] = 0, \qquad z = a, \tag{14c}$$

defines the Upper Layer Dirichlet–Neumann Operator

$$G(g) : U \to \tilde{U} := -(\partial_N u)(x, g(x)). \tag{15}$$

To simulate the DNO numerically we appeal to the TFE method [46,50] which begins with a domain–flattening change of variables (the σ–coordinates of oceanography [53] and the C–method of the dynamical theory of gratings [16,15])

$$x' = x, \quad z' = a\left(\frac{z - g(x)}{a - g(x)}\right).$$

With this we can rewrite the DNO problem, (14), in terms of the transformed field

$$u'(x', z') := u\left(x', \left(\frac{a - g(x')}{a}\right) z' + g(x')\right),$$

as (upon dropping primes)

$$\begin{aligned}
&\Delta u + 2i\alpha\partial_x u + (\gamma^u)^2 u = F(x,z), && 0 < z < a, && (16a)\\
&u(x,0) = U(x), && z = 0, && (16b)\\
&\partial_z u(x,a) - T^u[u(x,a)] = J(x), && z = a, && (16c)
\end{aligned}$$

and (15) as

$$G(g)[U] = -\partial_z u(x,0) + H(x). \tag{17}$$

The forms for $\{F, J, H\}$ have been derived and reported in [50] and, for brevity, we do not repeat them here.

Following our HOPS/AWE philosophy we assume the joint boundary/frequency perturbation

$$g(x) = \varepsilon f(x), \quad \omega = \underline{\omega} + \delta\underline{\omega},$$

and study the effect of this on (16) and (17). These become

$$\begin{aligned}
&\Delta u + 2i\underline{\alpha}\partial_x u + (\underline{\gamma}^u)^2 u = \tilde{F}(x,z), && 0 < z < a, && (18a)\\
&u(x,0) = U(x), && z = 0, && (18b)\\
&\partial_z u(x,a) - T_0^u[u(x,a)] = \tilde{J}(x), && z = a, && (18c)
\end{aligned}$$

and

$$G(\varepsilon f)[U] = -\partial_z u(x,0) + \tilde{H}(x). \tag{19}$$

In these

$$T_0^u[\xi(x)] := \sum_{p=-\infty}^{\infty} (i\underline{\gamma}_p^u)\hat{\xi}_p e^{i\tilde{p}x},$$

and

$$\begin{aligned}\tilde{F} = &-\varepsilon \text{div}\left[A_1(f)\nabla u\right] - \varepsilon^2 \text{div}\left[A_2(f)\nabla u\right] - \varepsilon B_1(f)\nabla u - \varepsilon^2 B_2(f)\nabla u \\ &- 2i\underline{\alpha}\delta\partial_x u - \delta^2(\underline{\gamma}^u)^2 u - 2\delta(\underline{\gamma}^u)^2 u \\ &- 2i\varepsilon S_1(f)\underline{\alpha}\partial_x u - 2i\varepsilon S_1(f)\underline{\alpha}\delta\partial_x u - \varepsilon S_1(f)\delta^2(\underline{\gamma}^u)^2 u \\ &- 2\varepsilon S_1(f)\delta(\underline{\gamma}^u)^2 u - \varepsilon S_1(f)(\underline{\gamma}^u)^2 u \\ &- 2i\varepsilon^2 S_2(f)\underline{\alpha}\partial_x u - 2i\varepsilon^2 S_2(f)\underline{\alpha}\delta\partial_x u - \varepsilon^2 S_2(f)\delta^2(\underline{\gamma}^u)^2 u \\ &- 2\varepsilon^2 S_2(f)\delta(\underline{\gamma}^u)^2 u - \varepsilon^2 S_2(f)(\underline{\gamma}^u)^2 u, \end{aligned} \tag{20}$$

and

$$\tilde{J} = -\frac{1}{a}(\varepsilon f(x))T^u\left[u(x,a)\right] + \left(T^u - T_0^u\right)\left[u(x,a)\right], \tag{21}$$

and

$$\tilde{H} = \varepsilon(\partial_x f)\partial_x u(x,0) + \varepsilon\frac{f}{a}G(\varepsilon f)[U] - \varepsilon^2\frac{f(\partial_x f)}{a}\partial_x u(x,0) - \varepsilon^2(\partial_x f)^2\partial_z u(x,0). \tag{22}$$

It is not difficult to see that the forms for the A_j, B_j, and S_j are

$$\begin{aligned} A_0 &= \begin{pmatrix} 1 & 0 \\ 0 & 1 \end{pmatrix}, \\ A_1(f) &= \frac{1}{a}\begin{pmatrix} -2f & -(a-z)(\partial_x f) \\ -(a-z)(\partial_x f) & 0 \end{pmatrix}, \\ A_2(f) &= \frac{1}{a^2}\begin{pmatrix} f^2 & (a-z)f(\partial_x f) \\ (a-z)f(\partial_x f) & (a-z)^2(\partial_x f)^2 \end{pmatrix}, \end{aligned}$$

and

$$B_1(f) = \frac{1}{a}\begin{pmatrix} \partial_x f \\ 0 \end{pmatrix}, \quad B_2(f) = \frac{1}{a^2}\begin{pmatrix} -f(\partial_x f) \\ -(a-z)(\partial_x f)^2 \end{pmatrix},$$

and

$$S_0 = 1, \quad S_1(f) = -\frac{2}{a}f, \quad S_2(f) = \frac{1}{a^2}f^2.$$

At this point we posit the expansions

$$u(x,z;\varepsilon,\delta) = \sum_{n=0}^{\infty}\sum_{m=0}^{\infty} u_{n,m}(x,z)\varepsilon^n\delta^m, \quad G(\varepsilon,\delta) = \sum_{n=0}^{\infty}\sum_{m=0}^{\infty} G_{n,m}\varepsilon^n\delta^m,$$

and, upon insertion into (18) and (19), we find

$$\Delta u_{n,m} + 2i\underline{\alpha}\partial_x u_{n,m} + (\underline{\gamma}^u)^2 u_{n,m} = \tilde{F}_{n,m}(x,z), \qquad 0 < z < a, \tag{23a}$$

$$u_{n,m}(x,0) = \delta_{n,0}\delta_{m,0}U(x), \qquad z = 0, \tag{23b}$$

$$\partial_z u_{n,m}(x,a) - T_0^u[u_{n,m}(x,a)] = \tilde{J}_{n,m}(x), \qquad z = a, \tag{23c}$$

and

$$G_{n,m}(f) = -\partial_z u_{n,m}(x,0) + \tilde{H}_{n,m}(x). \tag{24}$$

The formulas for $\tilde{F}_{n,m}$, $\tilde{J}_{n,m}$ and $\tilde{H}_{n,m}$ can be readily derived from (20), (21), and (22) above (see [33]).

Remark 1 In a forthcoming publication [33] we will use the recursions (23) and (24) to establish the *joint* analyticity of the DNO with respect to both interfacial and frequency deformations.

5.1 Joint Expansion of Surface Data

In order to specify forms for the surface data, $\{\zeta_{n,m}, \psi_{n,m}\}$, we require some results from [43]. First we recall the Taylor series expansion of the quantity γ_p^q, (3), with respect to δ away from a Rayleigh singularity (Wood anomaly) $\underline{\gamma}_p^q = 0$.

Lemma 1 *[43] The quantity γ_p^q has Taylor series expansion*

$$\gamma_p^q(\delta) = \sum_{m=0}^{\infty} \gamma_{p,m}^q \delta^m, \quad q \in \{u, w\},$$

where

$$\gamma_{p,0}^q = \pm \underline{\gamma}_p^q,$$

which we assume to be non–zero, giving rise to

$$\gamma_{p,1}^q = \frac{2((\underline{k}^q)^2 - \underline{\alpha}\;\underline{\alpha}_p)}{2\gamma_{p,0}^q}, \quad \gamma_{p,2}^q = \frac{(\underline{\gamma}^q)^2 - (\gamma_{p,1}^q)^2}{2\gamma_{p,0}^q},$$

$$\gamma_{p,m}^q = \frac{-\sum_{r=1}^{m-1} \gamma_{p,m-r}^q \gamma_{p,r}^q}{2\gamma_{p,0}^q}, \quad m > 2.$$

Remark 2 As we noted in [43] we must be *away* from a Rayleigh singularity, $\underline{\gamma}_p^q = 0$, for *all* p in order for our expansion to be valid. See the final section of [43] for a discussion of the behavior of the function $\gamma_p^q(\delta)$ in the neighborhood of a Rayleigh singularity.

Next we require the expansion of the composition of the exponential function with the product of a function of ε and a function of δ *jointly* in ε and δ.

Lemma 2 *[43] Let $\mathcal{E}(g, V) := \exp(g(x)V(\delta))$ for a function $g(x)$ and an analytic function*

$$V = V(\delta) = \sum_{m=0}^{\infty} V_m \delta^m.$$

The composite function $\mathcal{E}(g, V) = \mathcal{E}(\varepsilon f, V(\delta))$ is jointly analytic and has the Taylor series expansion

$$\mathcal{E}(\varepsilon, \delta) = \sum_{n=0}^{\infty} \sum_{m=0}^{\infty} \mathcal{E}_{n,m} \varepsilon^n \delta^m,$$

where

$$\mathcal{E}_{n,m} = \begin{cases} 1, & n = m = 0, \\ 0, & n = 0, m > 0, \\ (V_0)^n \frac{f^n}{n!}, & n > 0, m = 0, \\ \frac{f}{n+1} \sum_{r=0}^{m} \mathcal{E}_{n,m-r} V_r, & n, m > 0. \end{cases}$$

Remark 3 We note that this latter lemma can be effectively used to compute the expansions of the functions

$$e^{\pm i\gamma_p^q(\delta)\varepsilon f} = \mathcal{E}_p(\varepsilon f, \pm i\gamma_p^q(\delta)) = \mathcal{E}_p^{q,\pm}(\varepsilon, \delta) = \sum_{n=0}^{\infty} \sum_{m=0}^{\infty} \mathcal{E}_{p,n,m}^{q,\pm} \varepsilon^n \delta^m, \quad q \in \{u, w\},$$

which we presently require.

Using this lemma we find Taylor expansions for the data generated by plane–wave incidence (1e) and (1f). More specifically, for

$$\zeta = \sum_{n=0}^{\infty} \sum_{m=0}^{\infty} \zeta_{n,m} \varepsilon^n \delta^m, \quad \psi = \sum_{n=0}^{\infty} \sum_{m=0}^{\infty} \psi_{n,m} \varepsilon^n \delta^m,$$

we have

$$\begin{aligned} \zeta_{n,m} &= -\mathcal{E}_{0,n,m}^{u,-}, \\ \psi_{n,m} &= \sum_{r=0}^{m} (i\gamma_{p,m-r}^u) \mathcal{E}_{0,n,r}^{u,-} + (\partial_x f)(i\underline{\alpha}) \mathcal{E}_{0,n-1,m}^{u,-} + (\partial_x f)(i\underline{\alpha}) \mathcal{E}_{0,n-1,m-1}^{u,-}. \end{aligned}$$

6 Numerical Results

We are now in a position to test a numerical implementation of our method and demonstrate its advantageous computational complexity. Regarding the algorithm, our HOPS/AWE scheme is a High–Order Spectral method [25,6, 58] in the same spirit as our related TFE algorithm [50], where nonlinearities are approximated with convolutions implemented via the fast Fourier transform (FFT) algorithm. To test its validity we compare simulations from our implementation of this HOPS/AWE method to exact solutions constructed from the Method of Manufactured Solutions.

6.1 Implementation

As we mentioned above, our formulation of the scattering problem is

$$\mathbf{A}(\varepsilon, \delta)\mathbf{V}(\varepsilon, \delta) = \mathbf{R}(\varepsilon, \delta),$$

c.f. (9), and our HOPS/AWE approach asks for the joint expansion of the $\{\mathbf{A}, \mathbf{V}, \mathbf{R}\}$ in Taylor series, c.f. (11), where the $\{\mathbf{V}_{n,m}\}$ satisfy equation (12). In our approximation we begin by truncating the Taylor series

$$\begin{aligned}\{\mathbf{A}, \mathbf{V}, \mathbf{R}\}(\varepsilon, \delta) &\approx \{\mathbf{A}^{N,M}, \mathbf{V}^{N,M}, \mathbf{R}^{N,M}\}(\varepsilon, \delta) \\ &:= \sum_{n=0}^{N} \sum_{m=0}^{M} \{\mathbf{A}_{n,m}, \mathbf{V}_{n,m}, \mathbf{R}_{n,m}\} \varepsilon^n \delta^m, \end{aligned} \tag{25}$$

and all that remains is to specify (i.) how the forms $\mathbf{A}_{n,m}$ and $\mathbf{R}_{n,m}$ in (13) are simulated, and (ii.) how the operator $\mathbf{A}_{0,0}$ is to be inverted.

For the latter we note that $\mathbf{A}_{0,0}$ is diagonalized by the Fourier transform so that $\mathbf{A}_{0,0}\mathbf{V}_{n,m} = \mathbf{R}_{n,m}$ can be expressed as

$$\sum_{p=-\infty}^{\infty} \widehat{\mathbf{A}}_{0,0}(p) \widehat{\mathbf{V}}_{n,m}(p) e^{i\tilde{p}x} = \sum_{p=-\infty}^{\infty} \widehat{\mathbf{R}}_{n,m}(p) e^{i\tilde{p}x},$$

which implies

$$\widehat{\mathbf{V}}_{n,m}(p) = \left[\widehat{\mathbf{A}}_{0,0}(p)\right]^{-1} \widehat{\mathbf{R}}_{n,m}(p).$$

It is not difficult to see [42] that

$$\widehat{\mathbf{A}}_{0,0}(p) = \begin{pmatrix} 1 & -1 \\ (-i\gamma_p^u) & \tau^2(-i\gamma_p^w) \end{pmatrix},$$

c.f. (13), implying that

$$\left[\widehat{\mathbf{A}}_{0,0}(p)\right]^{-1} = \frac{1}{\Delta_p} \begin{pmatrix} \tau^2(-i\gamma_p^w) & 1 \\ (i\gamma_p^u) & 1 \end{pmatrix}, \quad \Delta_p := -(i\gamma_p^u + \tau^2(i\gamma_p^w)).$$

Remark 4 From these formulas it becomes obvious that the operator $\mathbf{A}_{0,0}$ is always invertible and our algorithm is well–defined. Recalling that we assume a dielectric in the upper layer (so that the incident radiation propagates) we have that γ_p^u is either real and positive or purely imaginary (with positive imaginary part). If a dielectric fills the lower layer then we have the same state of affairs for γ_p^w so that, given that τ^2 will be positive and real, $\Delta_p \neq 0$. Alternatively, if a metal fills the lower layer then γ_p^w will be complex with positive imaginary part. While it is less obvious, this ensures that, once again, $\Delta_p \neq 0$.

Regarding the forms $\mathbf{A}_{n,m}$ and $\mathbf{R}_{n,m}$, these boil down to the simulation of the terms $G_{n,m}$ and $J_{n,m}$ in Taylor series approximations of the DNOs, G and J. There is a large literature on the simulation of these operators in the case of a *boundary* perturbation alone (see, e.g., [47]), however, a novelty of our current work is the approximation of these DNOs *jointly* in interface and frequency deformation from the recursions found in Section 5. As we presently describe, the method is very similar to that presented in [47] save that additional elliptic solves are required.

6.2 A Fourier/Chebyshev Collocation Discretization

Focusing on the upper layer DNO, G, we begin by approximating

$$u(x,z;\varepsilon,\delta) \approx u^{N,M}(x,z;\varepsilon,\delta) := \sum_{n=0}^{N} \sum_{m=0}^{M} u_{n,m}(x,z) \varepsilon^n \delta^m.$$

Each of these $u_{n,m}(x,z)$ are then simulated by a Fourier–Chebyshev approach which posits the form

$$u_{n,m}(x,z) \approx u_{n,m}^{N_x,N_z}(x,z) := \sum_{p=-N_x/2}^{N_x/2-1} \sum_{\ell=0}^{N_z} \hat{u}_{n,m,p,\ell} e^{i\tilde{p}x} T_\ell \left(\frac{2z-a}{a} \right),$$

where T_ℓ is the ℓ–th Cheybshev polynomial. The unknowns, $\hat{u}_{n,m,p,\ell}$ are recovered from (23) by the collocation approach [25,14,6,58,59]. With this we can simulate the upper layer DNO from (24), giving

$$G(x;\varepsilon,\delta) \approx G^{N,M}(x;\varepsilon,\delta) := \sum_{n=0}^{N} \sum_{m=0}^{M} G_{n,m}(x) \varepsilon^n \delta^m,$$

where

$$G_{n,m}(x) \approx G_{n,m}^{N_x}(x) := \sum_{p=-N_x/2}^{N_x/2-1} \hat{G}_{n,m,p} e^{i\tilde{p}x}, \qquad (26)$$

and the $\hat{G}_{n,m,p}$ are recovered from the $\hat{u}_{n,m,p,\ell}$.

6.3 Padé Approximation

We conclude our discussion of implementation with consideration of how the Taylor series in (ε,δ) are summed. For example, regarding the DNO, G, the approximation of $\hat{G}_p(\varepsilon,\delta)$ by

$$\hat{G}_p^{N,M}(\varepsilon,\delta) := \sum_{n=0}^{N} \sum_{m=0}^{M} \hat{G}_{n,m,p} \varepsilon^n \delta^m,$$

c.f. (26). The technique of Padé approximation [3] has been used with HOPS methods to great advantage in the past [8,48] and we advocate its use here. Classically, this approach seeks to estimate the truncated Taylor series of a *single* variable

$$Q^N(\rho) := \sum_{n=0}^{N} Q_n \rho^n \approx Q(\rho),$$

by the rational function

$$[L/M](\rho) := \frac{a^L(\rho)}{b^M(\rho)} = \frac{\sum_{\ell=0}^{L} a_\ell \rho^\ell}{1 + \sum_{m=1}^{M} b_m \rho^m}, \quad L + M = N,$$

and

$$[L/M](\rho) = Q^N(\rho) + \mathcal{O}(\rho^{L+M+1});$$

well–known formulas for the coefficients $\{a_\ell, b_m\}$ can be found in [3]. Padé approximation enjoys greatly enhanced convergence properties and we refer the interested reader to § 2.2 of Baker & Graves–Morris [3] and the insightful calculations of § 8.3 of Bender & Orszag [4] for a thorough discussion of the capabilities and limitations of Padé approximants.

In the current context of functions analytic with respect to *two* perturbation variables we utilize the polar coordinates

$$\varepsilon = \rho\cos(\theta), \quad \delta = \rho\sin(\theta),$$

and write the function

$$\begin{aligned}\hat{G}_p(\varepsilon,\delta) &= \sum_{n=0}^{\infty}\sum_{m=0}^{\infty} \hat{G}_{n,m,p}\varepsilon^n\delta^m \\ &= \sum_{n=0}^{\infty}\sum_{m=0}^{\infty} \left(\hat{G}_{n,m,p}\cos^n(\theta)\sin^m(\theta)\right)\rho^{n+m}.\end{aligned}$$

Setting $\ell = n + m$ and $s = m$ we can write this as

$$\hat{G}_p(\varepsilon,\delta) = \sum_{\ell=0}^{\infty}\left\{\sum_{s=0}^{\ell} \hat{G}_{\ell-s,s,p}\cos^{\ell-s}(\theta)\sin^s(\theta)\right\}\rho^\ell =: \sum_{\ell=0}^{\infty}\tilde{G}_{\ell,p}(\theta)\rho^\ell.$$

We then chose particular values of $\theta = \theta_j$ between 0 and 2π and used classical Padé approximation on the resulting $\{\tilde{G}_{\ell,p}(\theta_j)\}$ as a function of ρ alone.

6.4 The Domain of Analyticity

In a forthcoming publication [33] we will rigorously demonstrate the *joint* analyticity of the fields, $\{u, w\}$, DNOs, $\{G, J\}$, and solutions, $\{U, W\}$, with respect to both boundary, ε, and frequency perturbations, δ. As we have mentioned on several occasions, the implicit smallness assumption on ε may be safely dropped upon consideration of our previous work [47,48,51,28]. However, it is clear that no such extension exists for δ as we have already seen how the expansion for $\gamma_p^q(\delta)$ fails at a Rayleigh Singularity, $\underline{\gamma}_p^q = 0$, c.f. Lemma 1. Therefore the permissible values of δ *must* be constrained by this.

To guide our computations we explore this restriction on δ in more detail. For instance, in the upper layer, Rayleigh singularities occur when $\underline{\alpha}_p^2 = (\underline{k}^u)^2$ which implies

$$\underline{\omega} = \pm\frac{c_0}{n^u}\left\{\underline{\alpha} + \frac{2\pi p}{d}\right\}, \quad \text{for any } p \in \mathbf{Z}. \tag{27}$$

In the interest of maximizing our choice of δ we select a "mid–point" value of $\underline{\omega}$ which is as far away as possible from consecutive Rayleigh singularities

$$\underline{\omega}_q := \frac{c_0}{n^u} \left\{ \underline{\alpha} + \frac{2\pi(q+1/2)}{d} \right\}. \tag{28}$$

About this value the nearest singularities are

$$\begin{aligned} \underline{\omega}_q^- &:= \frac{c_0}{n^u} \left\{ \underline{\alpha} + \frac{2\pi q}{d} \right\} = \underline{\omega}_q - \frac{\pi c_0}{n^u d}, \\ \underline{\omega}_q^+ &:= \frac{c_0}{n^u} \left\{ \underline{\alpha} + \frac{2\pi(q+1)}{d} \right\} = \underline{\omega}_q + \frac{\pi c_0}{n^u d}, \end{aligned}$$

so to maximize our range of ω we choose, for some filling fraction $0 < \sigma < 1$,

$$\underline{\omega}_q - \sigma \left(\frac{\pi c_0}{n^u d} \right) < \omega < \underline{\omega}_q + \sigma \left(\frac{\pi c_0}{n^u d} \right). \tag{29}$$

To express this in terms of δ we recall that $\omega = (1+\delta)\underline{\omega}_q$ which gives

$$-\sigma \left(\frac{\pi c_0}{\underline{\omega}_q n^u d} \right) < \delta < \sigma \left(\frac{\pi c_0}{\underline{\omega}_q n^u d} \right).$$

Simplifying gives

$$-\left(\frac{\sigma}{(\underline{\alpha} d/\pi) + 2q + 1} \right) < \delta < \left(\frac{\sigma}{(\underline{\alpha} d/\pi) + 2q + 1} \right). \tag{30}$$

6.5 Validation by the Method of Manufactured Solutions

To validate our scheme we utilized the Method of Manufactured Solutions [13,55,56]. To summarize, consider the general system of partial differential equations subject to generic boundary conditions

$$\begin{aligned} \mathcal{P} v &= 0, && \text{in } \Omega, \\ \mathcal{B} v &= 0, && \text{at } \partial\Omega. \end{aligned}$$

It is typically easy to implement a numerical algorithm to solve the nonhomogeneous version of this set of equations

$$\begin{aligned} \mathcal{P} v &= \mathcal{F}, && \text{in } \Omega, \\ \mathcal{B} v &= \mathcal{J}, && \text{at } \partial\Omega. \end{aligned}$$

To test an implementation we began with the "manufactured solution," $\tilde{v}$, and set

$$\mathcal{F}_v := \mathcal{P}\tilde{v}, \quad \mathcal{J}_v := \mathcal{J}\tilde{v}.$$

Thus, given the pair $\{\mathcal{F}_v, \mathcal{J}_v\}$ we had an *exact* solution of the nonhomogeneous problem, namely $\tilde{v}$. While this does not prove an implementation to be correct, if the function $\tilde{v}$ is chosen to imitate the behavior of anticipated solutions (e.g., satisfying the boundary conditions exactly) then this gives us confidence in our algorithm.

We considered the periodic, outgoing solutions of the Helmholtz equation (6a)

$$u_r(x,z) := A_r e^{i\tilde{r}x + i\gamma_r^u z}, \quad r \in \mathbf{Z}, \quad A_r \in \mathbf{C},$$

and their counterparts for (6b)

$$w_r(x,z) := B_r e^{i\tilde{r}x - i\gamma_r^w z}, \quad r \in \mathbf{Z}, \quad B_r \in \mathbf{C}.$$

We selected the simple sinusoidal profile

$$g(x) = \varepsilon f(x) = \varepsilon \left(\frac{\cos(4x)}{4} \right), \tag{31}$$

and defined the Dirichlet and Neumann traces

$$U_r(x) := u_r(x, g(x)), \quad \tilde{U}_r(x) := -\partial_N u_r(x, g(x)), \tag{32a}$$

$$W_r(x) := w_r(x, g(x)), \quad \tilde{W}_r(x) := \partial_N w_r(x, g(x)). \tag{32b}$$

From these we defined the two–layer data to be provided to our algorithm

$$\zeta_r := U_r - W_r, \quad \psi_r := -\tilde{U}_r - \tau^2 \tilde{W}_r. \tag{32c}$$

We chose the following physical parameters

$$d = 2\pi, \quad \alpha = 0, \quad \epsilon^u = 1, \quad \epsilon^w = 1.1, \quad r = 4, \quad A_r = 5, \quad B_r = 3, \tag{33}$$

in TM polarization, and the numerical parameters

$$N_x = 32, \quad N_z = 32, \quad a = 1, \quad b = -1. \tag{34}$$

With a rescaling of the frequency (e.g., via a change of the time variable, $t' = t/c_0$) we arrange for $c_0 = 1$ and considered the base frequency

$$\underline{\omega}_1 = 3/2,$$

and filling fraction $\sigma = 0.99$.

To illuminate the behavior of our scheme we studied four choices of the numerical parameter

$$N = M = 4, 8, 12, 16,$$

and the physical quantities

$$\varepsilon = 10^{-2}, 10^{-4}, 10^{-6}, 10^{-8},$$

in (31). For this we supplied the "exact" input data, $\{\zeta_r, \psi_r\}$, from (32) to our HOPS/AWE algorithm to simulate solutions of the two–layer problem giving $\{U_r^{\text{approx}}, W_r^{\text{approx}}\}$. We compared this with the "exact" solutions $\{U_r^{\text{exact}}, W_r^{\text{exact}}\}$ and computed the relative error

$$\text{Error}_{\text{rel}} := \frac{|U_r^{\text{exact}} - U_r^{\text{approx}}|_{L^\infty}}{|U_r^{\text{exact}}|_{L^\infty}}.$$

We point out that measuring the defect in the upper–layer Dirichlet data was arbitrary and we noticed similar behavior for the lower–layer analogue.

We report our results of these simulations in Figures 2 and 3. More specifically, Figure 2 displays both the rapid and stable decay of the relative error for fixed N and M, and how this rate of decay improves as (ε, δ) decrease. Figure 3 shows both how the error shrinks as (ε, δ) become smaller, and that this rate is enhanced as both N and M are increased.

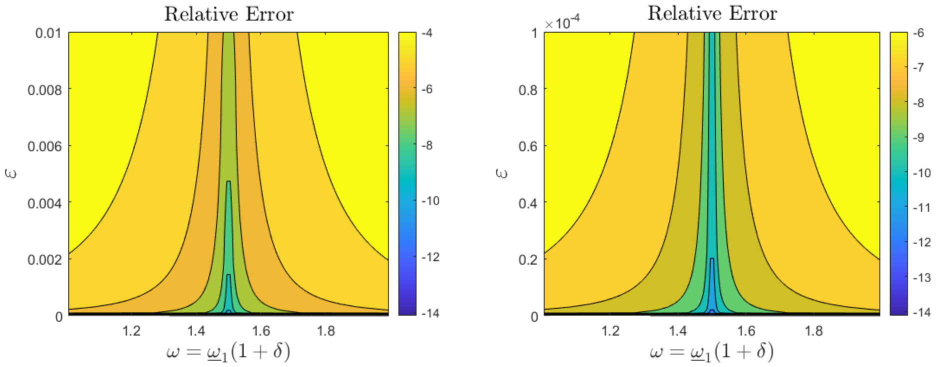

(a) $N = M = 4, \varepsilon = 10^{-2}$ (b) $N = M = 4, \varepsilon = 10^{-4}$

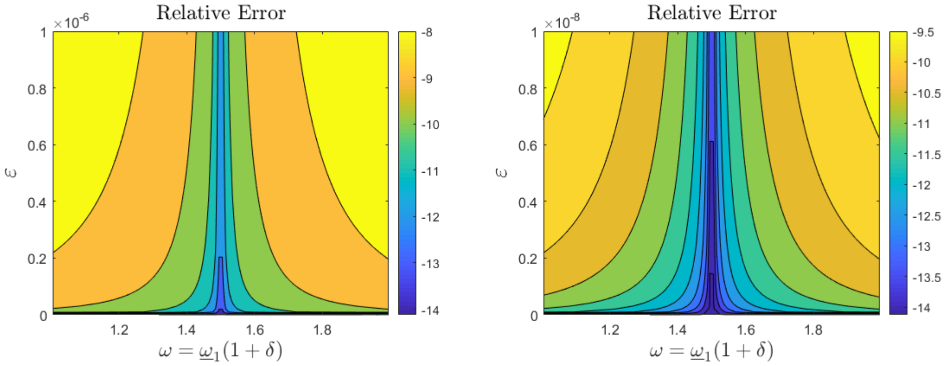

(c) $N = M = 4, \varepsilon = 10^{-6}$ (d) $N = M = 4, \varepsilon = 10^{-8}$

Fig. 2: Plot of relative error with fixed $N = M = 4$ and four choices of $\varepsilon = 10^{-2}, 10^{-4}, 10^{-6}, 10^{-8}$ with Taylor summation. Physical parameters were (33) and numerical discretization was (34).

To further explore the capabilities and limitations of our numerical scheme we conducted simulations for boundary deformations of large size and low smoothness following the guidance of our previous work in [47] on HOPS algorithms. For this we considered the first frequency/wavelength range in (29), $q = 1$, TM polarization, and two–dimensional domains whose upper/lower

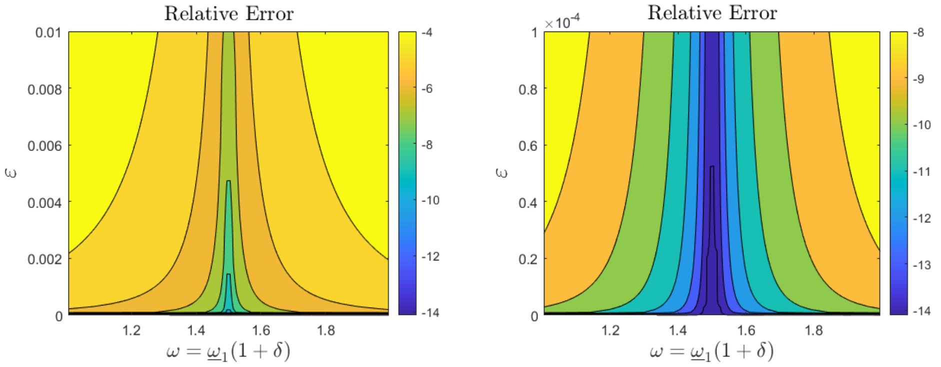

(a) $N = M = 4, \varepsilon = 10^{-2}$ (b) $N = M = 8, \varepsilon = 10^{-4}$

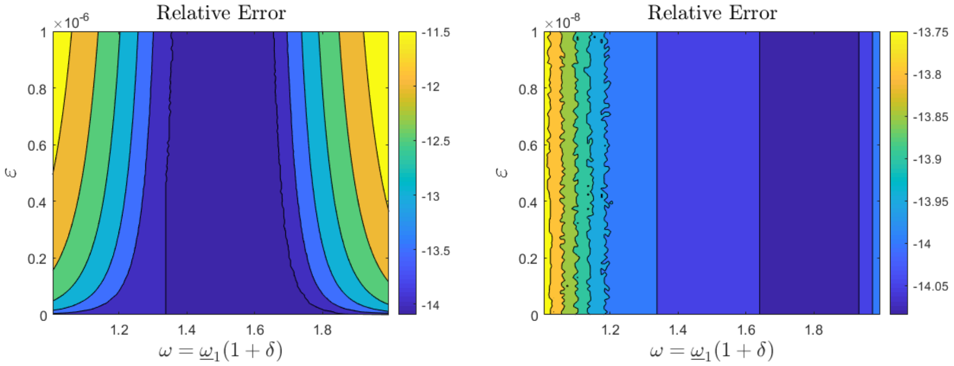

(c) $N = M = 12, \varepsilon = 10^{-6}$ (d) $N = M = 16, \varepsilon = 10^{-8}$

Fig. 3: Plot of relative error with four choices of $N = M = 4, 8, 12, 16$ and four choices of $\varepsilon = 10^{-2}, 10^{-4}, 10^{-6}, 10^{-8}$ with Taylor summation. Physical parameters were (33) and numerical discretization was (34).

boundaries are shaped by the profiles

$$f_s(x) = \frac{\cos(4x)}{4}, \tag{35a}$$

$$f_r(x) = \left(2 \times 10^{-4}\right) x^4 \left(2\pi - x^4\right) - c_0, \tag{35b}$$

$$f_L(x) = \begin{cases} -2x/\pi + 1, & 0 \le x \le \pi, \\ 2x/\pi - 3, & \pi \le x \le 2\pi, \end{cases} \tag{35c}$$

where f_s, f_r, and f_L represent boundaries which are smooth (C^∞), rough (finite smoothness, C^4), and Lipschitz, respectively. Following [47], the constant c_0 in (35b) is chosen so that (like f_s and f_L) f_r has zero mean. As shown in

[47] the Fourier series representations of f_r and f_L are

$$
\begin{aligned}
f_r(x) &= \sum_{k=1}^{\infty} \frac{96\left(2k^2\pi^2 - 21\right)}{125k^8} \cos(kx), && \text{(36a)}\\
f_L(x) &= \sum_{k=1}^{\infty} \frac{8}{\pi^2(2k-1)^2} \cos\big((2k-1)x\big), && \text{(36b)}
\end{aligned}
$$

respectively. To minimize the effect of aliasing errors we approximated f_r and f_L by the truncated Fourier series

$$
\begin{aligned}
f_{r,P}(x) &= \sum_{k=1}^{P} \frac{96\left(2k^2\pi^2 - 21\right)}{125k^8} \cos(kx), && \text{(37a)}\\
f_{L,P}(x) &= \sum_{k=1}^{P/2} \frac{8}{\pi^2(2k-1)^2} \cos\big((2k-1)x\big). && \text{(37b)}
\end{aligned}
$$

If $P \ll N_x/2$ then the effects of aliasing are minimal and we chose $P = 120$ for all of our simulations.

In order to test the capabilities of our algorithm we performed simulations with these profiles for large values of ε and report our findings for the maximum value which produced reliable results. For the smooth profile, we selected

$$
\begin{gathered}
\varepsilon_{\max} = 2.0, \quad a = 4, \quad b = -4,\\
\alpha = 0, \quad \sigma = 0.99, \quad n^u = 1, \quad n^w = 1.1,\\
N_x = 256, \quad N_z = 128, \quad N = M = 20,
\end{gathered} \tag{38}
$$

and for the rough and Lipschitz profiles, we chose

$$
\begin{gathered}
\varepsilon_{\max} = 2.0, \quad a = 4, \quad b = -4,\\
\alpha = 0, \quad \sigma = 0.99, \quad n^u = 1, \quad n^w = 1.1,\\
N_x = 1024, \quad N_z = 128, \quad N = M = 20.
\end{gathered} \tag{39}
$$

We report the results of these simulations in Figures 4, 5, and 6. Here we notice how, with a modest number of perturbation orders ($N = M = 20$) we can very accurately simulate the upper layer Dirichlet data (with relative errors at most 10^{-7}) with a quite reasonable number of unknowns, $N_x = 256$ (f_s) or $N_x = 1024$ ($f_{r,P}$ and $f_{L,P}$) and $N_z = 128$. As the period in this case is 2π we see how our algorithm can handle profiles of slope above 30% whose smoothness is nearly the minimum required for our analyticity results, merely Lipschitz.

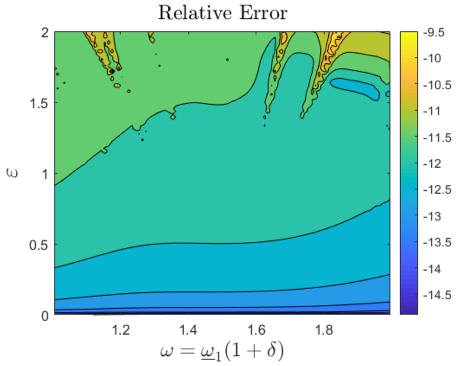

Fig. 4: The relative error for f_s computed with our HOPS/AWE algorithm with Padé summation. We set $N = M = 20$ with a granularity of $N_\varepsilon = N_\delta = 100$ per invocation. Parameter choices were $\alpha = 0$, $\sigma = 0.99$, $n^u = 1$, $n^w = 1.1$, $N_x = 256$, and $N_z = 128$.

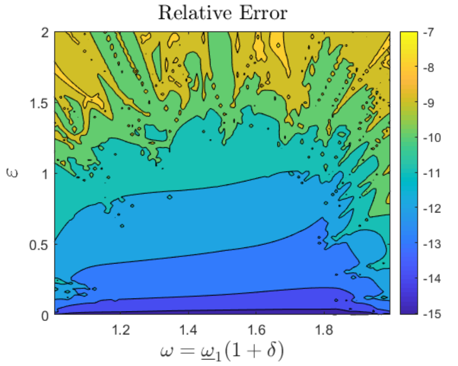

Fig. 5: The relative error for $f_{r,P}$ computed with our HOPS/AWE algorithm with Padé summation. We set $N = M = 20$ with a granularity of $N_\varepsilon = N_\delta = 100$ per invocation. Parameter choices were $\alpha = 0$, $\sigma = 0.99$, $n^u = 1$, $n^w = 1.1$, $N_x = 1024$, and $N_z = 128$.

6.6 Simulations of the Reflectivity Maps

In Section 2.2 we defined the Reflectivity Map $R = R(\varepsilon, \delta)$, c.f. (7). Using our novel HOPS/AWE approach we computed

$$R^{N,M,N_x,N_z}_{\text{HOPS/AWE}} \approx R,$$

for a range of ε and δ. As in our previous work [43], we show the kind of simulations this HOPS/AWE method can produce with modest computational effort. For this we selected $\underline{\omega}_q$, c.f. (28), for $1 \le q \le 6$ and simulated R in the

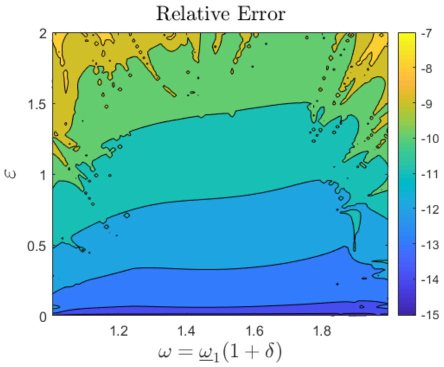

Fig. 6: The relative error for $f_{L,P}$ computed with our HOPS/AWE algorithm with Padé summation. We set $N = M = 20$ with a granularity of $N_\varepsilon = N_\delta = 100$ per invocation. Parameter choices were $\alpha = 0$, $\sigma = 0.99$, $n^u = 1$, $n^w = 1.1$, $N_x = 1024$, and $N_z = 128$.

following frequency/wavelength ranges

$$\begin{aligned}
q = 1: &\quad \omega \in [1.005, 1.995] &\implies&\quad \lambda \in [3.14947, 6.25193],\\
q = 2: &\quad \omega \in [2.005, 2.995] &\implies&\quad \lambda \in [2.09789, 3.13376],\\
q = 3: &\quad \omega \in [3.005, 3.995] &\implies&\quad \lambda \in [1.57276, 2.09091],\\
q = 4: &\quad \omega \in [4.005, 4.995] &\implies&\quad \lambda \in [1.25789, 1.56884],\\
q = 5: &\quad \omega \in [5.005, 5.995] &\implies&\quad \lambda \in [1.04807, 1.25538],\\
q = 6: &\quad \omega \in [6.005, 6.995] &\implies&\quad \lambda \in [0.89824, 1.04633],
\end{aligned}$$

c.f. (30). In addition, we selected

$$g(x) = \varepsilon f(x), \quad f(x) = \cos(x), \quad \varepsilon_{\max} = 0.2,$$

with the parameters

$$\alpha = 0, \quad \sigma = 0.99, \quad n^u = 1, \quad n^w = 1.1, \quad N_x = N_z = 32, \quad N = M = 16.$$

In Figure 7(a) we plot all six of these subsets of the Reflectivity Map on one set of coordinate axes, and in Figure 7(b) we plot the energy defect, D, (8), to verify the accuracy of our expansions.

We then changed the lower index of refraction n^w to match representative values of silver and gold as reported by Johnson & Christy [31], in particular

$$n_{\mathrm{Ag}} = 0.05 + 2.275i, \quad n_{\mathrm{Au}} = 1.48 + 1.883i.$$

Using the same frequency and wavelength ranges, we studied

$$f(x) = \cos(4x), \quad \varepsilon_{\max} = 0.2,$$

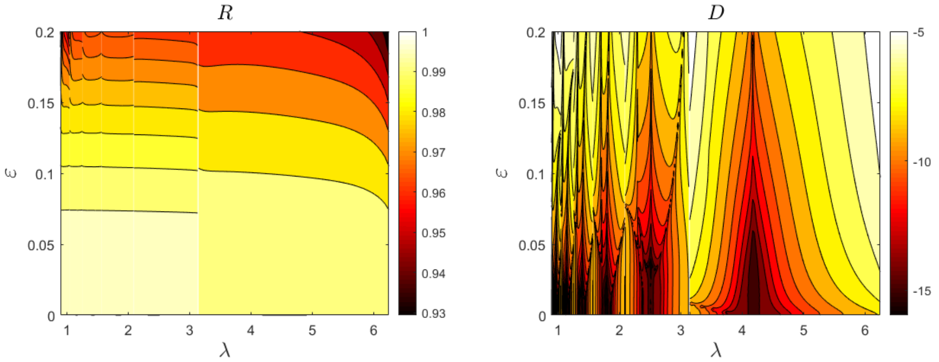

(a) Reflectivity Map (b) Energy Defect

Fig. 7: The Reflectivity Map, $R(\varepsilon, \delta)$, and energy defect, $D(\varepsilon, \delta)$, for $\cos(x)$ computed with our HOPS/AWE algorithm with Taylor summation. We set $N = M = 16$ with a granularity of $N_\varepsilon = N_\delta = 100$ per invocation. Parameter choices were $\alpha = 0$, $\sigma = 0.99$, $n^u = 1$, $n^w = 1.1$, and $N_x = N_z = 32$.

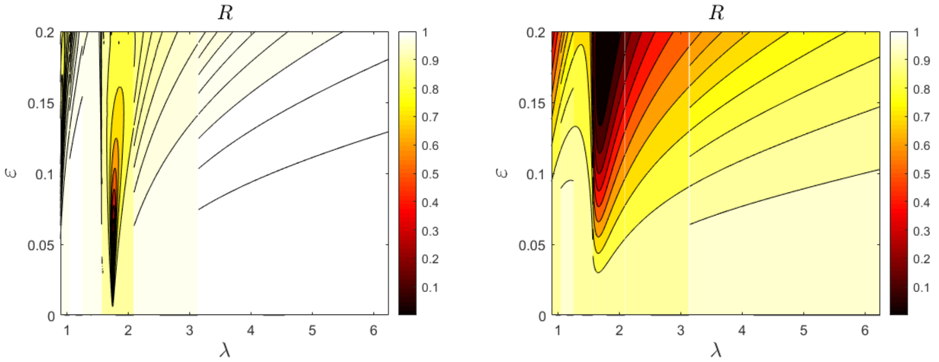

(a) Reflectivity Map for Silver (b) Reflectivity Map for Gold

Fig. 8: The Reflectivity Map, $R(\varepsilon, \delta)$, where $f(x) = \cos(4x)$ for silver (left) and gold (right) with Padé summation. We set $N = M = 15$ with a granularity of $N_\varepsilon = N_\delta = 100$ per invocation. Parameter choices were $\alpha = 0$, $\sigma = 0.99$, $n^u = 1$, $n^w = n_{\mathrm{Ag}}$ (left) and $n^w = n_{\mathrm{Au}}$ (right), $N_x = N_z = 32$, and the periodicity of the grating was selected as $d = 2\pi$.

with the parameters

$$\alpha = 0, \quad \sigma = 0.99, \quad n^u = 1, \quad N_x = N_z = 32, \quad N = M = 15.$$

In Figure 8(a) we plot six different subsets of the reflectivity map where the lower index of refraction is selected to model the optical constant of silver.

In Figure 8(b) we plot six different subsets of the Reflectivity Map where the lower index of refraction is changed to the optical constant for gold.

We now turn to simulations featuring our large smooth, rough, and Lipschitz profiles defined in (35) and approximated by (37) (with $P = 120$ in this contribution). As before, we worked in the first frequency/wavelength range, $q = 1$, in TM polarization with parameter choices (38) for the smooth interface and (39) for the rough and Lipschitz surfaces. We report the results of these simulations in Figures 9, 10 and 11 for the smooth, rough, and Lipschitz profiles, respectively. More specifically, Figure 9 displays the reflectivity map and energy defect for the smooth profile, while Figures 10 and 11 make the same comparison for the rough and Lipschitz profiles.

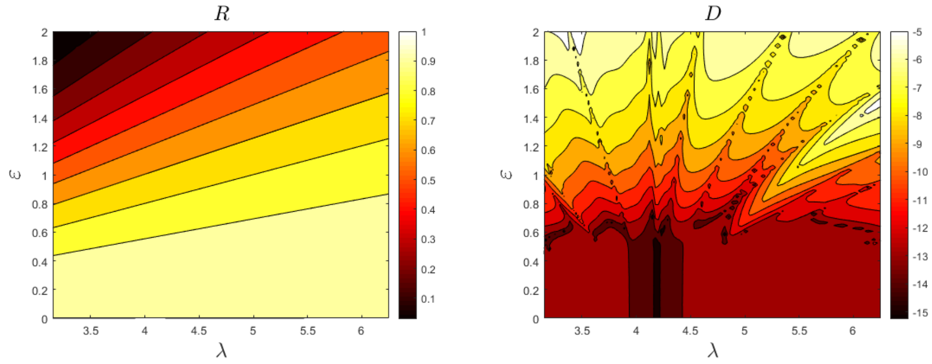

(a) Reflectivity Map

(b) Energy Defect

Fig. 9: The Reflectivity Map, $R(\varepsilon, \delta)$ and energy defect, $D(\varepsilon, \delta)$, for f_s computed with our HOPS/AWE algorithm with Padé summation. We set $N = M = 20$ with a granularity of $N_\varepsilon = N_\delta = 100$ per invocation. Parameter choices were $\alpha = 0$, $\sigma = 0.99$, $n^u = 1$, $n^w = 1.1$, $N_x = 256$, and $N_z = 128$.

We conclude with computations of the same configuration but with increased granularity, $N_\varepsilon = N_\delta = 1000$ per invocation. In the next section we discuss the advantageous computational complexity our HOPS/AWE algorithm enjoys in this situation of large N_ε and N_δ. We selected

$$f(x) = \cos(x), \quad \varepsilon_{\max} = 0.2,$$

with the parameters

$$\alpha = 0.01, \quad \sigma = 0.99, \quad n^u = 1, \quad n^w = 1.1, \quad N_x = N_z = 32, \quad N = M = 16.$$

In Figure 12(a) we plot six different subsets of the Reflectivity Map on a single coordinate axis, and in Figure 12(b) we plot the energy defect, (8), to demonstrate the accuracy of our scheme with a nonzero value of $\underline{\alpha}$.

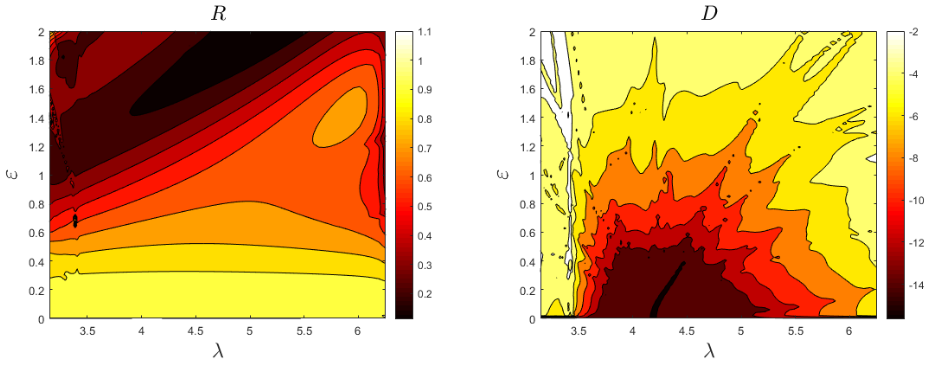

(a) Reflectivity Map

(b) Energy Defect

Fig. 10: The Reflectivity Map, $R(\varepsilon, \delta)$ and energy defect, $D(\varepsilon, \delta)$, for $f_{r,P}$ computed with our HOPS/AWE algorithm with Padé summation. We set $N = M = 20$ with a granularity of $N_\varepsilon = N_\delta = 100$ per invocation. Parameter choices were $\alpha = 0$, $\sigma = 0.99$, $n^u = 1$, $n^w = 1.1$, $N_x = 1024$, and $N_z = 128$.

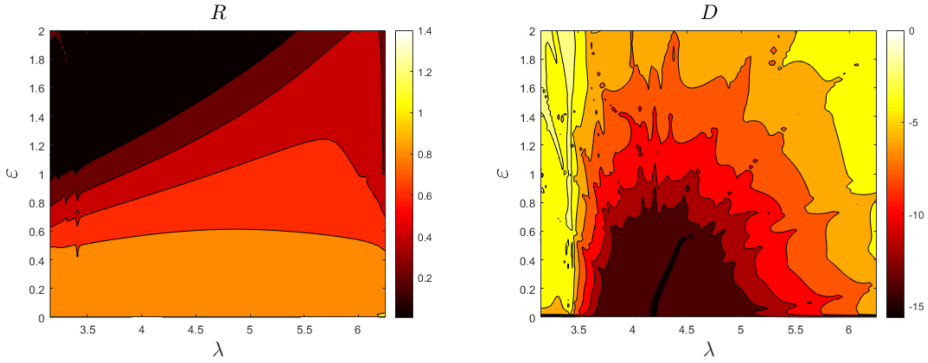

(a) Reflectivity Map

(b) Energy Defect

Fig. 11: The Reflectivity Map, $R(\varepsilon, \delta)$ and energy defect, $D(\varepsilon, \delta)$, for $f_{L,P}$ computed with our HOPS/AWE algorithm with Padé summation. We set $N = M = 20$ with a granularity of $N_\varepsilon = N_\delta = 100$ per invocation. Parameter choices were $\alpha = 0$, $\sigma = 0.99$, $n^u = 1$, $n^w = 1.1$, $N_x = 1024$, and $N_z = 128$.

6.7 Computational Complexity

One of the primary motivations for our HOPS/AWE algorithm is its superior computational complexity for problems within its domain of applicability. In comparison with classical BIE methods, for instance, the HOPS/AWE approach has several advantages for computing QoIs like the Reflectivity Map,

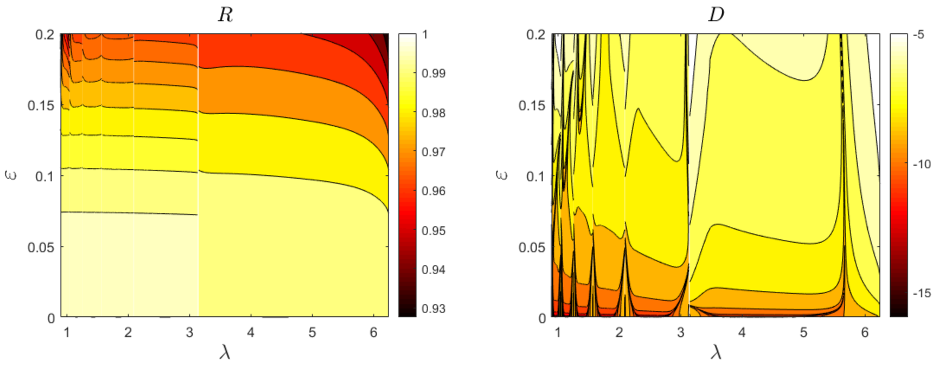

(a) Reflectivity Map (b) Energy Defect

Fig. 12: The Reflectivity Map, $R(\varepsilon, \delta)$, and energy defect, $D(\varepsilon, \delta)$, for $\cos(x)$ computed with our HOPS/AWE algorithm with Taylor summation. We set $N = M = 16$ with a granularity of $N_\varepsilon = N_\delta = 1000$ per invocation. Parameter choices were $\alpha = 0.01$, $\sigma = 0.99$, $n^u = 1$, $n^w = 1.1$, and $N_x = N_z = 32$.

$R = R(\varepsilon, \delta)$. To demonstrate this we begin by fixing the problem of computing R for N_ε many values of ε and N_δ many values of δ.

We recall from Section 6.2 that our HOPS/AWE algorithm requires $N_x \times N_z$ unknowns at every perturbation order, (n, m), corresponding to the N_x equally–spaced gridpoints in the lateral direction and the N_z collocation points in the vertical dimension. A careful study of the HOPS/AWE recursions (12) reveals that the computational complexity of *forming* the right–hand side at order (n, m) (the most costly step) is

$$\mathcal{O}(nmN_x \log(N_x)N_z \log(N_z)).$$

Inverting the operator $A_{0,0}$ has complexity $\mathcal{O}(N_x \log(N_x)N_z \log(N_z))$ so the full cost of computing the $\{U_{n,m}, W_{n,m}\}$, $\{0 \leq n \leq N, 0 \leq m \leq M\}$, is

$$\mathcal{O}(N^2M^2N_x \log(N_x)N_z \log(N_z)).$$

Once these coefficients are recovered, the cost of summing the series in (ε, δ) is minimal, provided it is done in an efficient manner (e.g., by Horner's rule [12,2]). Our algorithm then requires an additional $\mathcal{O}(N_\varepsilon N_\delta)$ steps to sum over every value of (ε, δ), therefore the *full* cost of computing the Reflectivity Map by our HOPS/AWE method is

$$\mathcal{O}(N^2M^2N_x \log(N_x)N_z \log(N_z) + N_\varepsilon N_\delta).$$

In contrast, for a single (ε, δ) pair, a BIM solver with N_x lateral gridpoints requires time proportional to $\mathcal{O}(N_x^3)$ for Gaussian elimination to solve the resulting *dense* system of N_x equations in N_x unknowns [12,2,17]. Applying this $N_\varepsilon \times N_\delta$ times results in a total computational complexity of

$$\mathcal{O}(N_x^3 N_\varepsilon N_\delta).$$

Thus, once N_ε and N_δ become large, e.g.,

$$N_\varepsilon N_\delta > \frac{N^2 M^2 N_x \log(N_x) N_z \log(N_z)}{N_x^3},$$

our new algorithm becomes far more efficient.

7 Conclusions

In this paper we have described a novel, High–Order Spectral [25,14] High–Order Perturbation of Surfaces (HOPS)/Asymptotic Waveform Evaluation (AWE) method [43] which employs a perturbation approach to address the geometric and frequency deviations from a base configuration. For quantities which depend upon both of these variables, such as the Reflectivity Map, this method enjoys extremely favorable computational complexity as compared with standard numerical methods such as Finite Differences, Finite Elements, and even Integral Equations. Our HOPS/AWE algorithm has been shown to be rapid, robust, and highly accurate.

Acknowledgments

D.P.N. gratefully acknowledges support from the National Science Foundation through grants No. DMS–1813033 and No. DMS–2111283.

Data Availability

The datasets generated during and/or analyzed during the current study are available from the corresponding author on reasonable request.

Declarations

All authors contributed to the study conception and design. Material preparation, data collection and analysis were performed by all authors. The first draft of the manuscript was written by Matthew Kehoe and all authors commented on previous versions of the manuscript. All authors read and approved the final manuscript.

References

1. Arens, T.: Scattering by biperiodic layered media: The integral equation approach. Habilitationsschrift, Karlsruhe Institute of Technology (2009)
2. Atkinson, K., Han, W.: Theoretical numerical analysis, *Texts in Applied Mathematics*, vol. 39. Springer-Verlag, New York (2001). A functional analysis framework
3. Baker Jr., G.A., Graves-Morris, P.: Padé approximants, second edn. Cambridge University Press, Cambridge (1996)
4. Bender, C.M., Orszag, S.A.: Advanced mathematical methods for scientists and engineers. McGraw-Hill Book Co., New York (1978). International Series in Pure and Applied Mathematics
5. Bleibinhaus, F., Rondenay, S.: Effects of surface scattering in full-waveform inversion. Geophysics **74**(6), WCC69–WCC77 (2009)
6. Boyd, J.P.: Chebyshev and Fourier spectral methods, second edn. Dover Publications Inc., Mineola, NY (2001)
7. Brekhovskikh, L.M., Lysanov, Y.P.: Fundamentals of Ocean Acoustics. Springer-Verlag, Berlin (1982)
8. Bruno, O., Reitich, F.: Numerical solution of diffraction problems: A method of variation of boundaries. II. Finitely conducting gratings, Padé approximants, and singularities. J. Opt. Soc. Am. A **10**(11), 2307–2316 (1993)
9. Bruno, O.P., Lyon, M., Pérez-Arancibia, C., Turc, C.: Windowed Green function method for layered-media scattering. SIAM J. Appl. Math. **76**(5), 1871–1898 (2016)
10. Bruno, O.P., Shipman, S.P., Turc, C., Venakides, S.: Superalgebraically convergent smoothly windowed lattice sums for doubly periodic Green functions in three-dimensional space. Proc. A. **472**(2191), 20160255, 19 (2016)
11. Bruno, O.P., Shipman, S.P., Turc, C., Venakides, S.: Three-dimensional quasi-periodic shifted Green function throughout the spectrum, including Wood anomalies. Proc. A. **473**(2207), 20170242, 18 (2017)
12. Burden, R., Faires, J.D.: Numerical analysis, sixth edn. Brooks/Cole Publishing Co., Pacific Grove, CA (1997)
13. Burggraf, O.R.: Analytical and numerical studies of the structure of steady separated flows. J. Fluid Mech. **24**, 113–151 (1966)
14. Canuto, C., Hussaini, M.Y., Quarteroni, A., Zang, T.A.: Spectral methods in fluid dynamics. Springer-Verlag, New York (1988)
15. Chandezon, J., Dupuis, M., Cornet, G., Maystre, D.: Multicoated gratings: a differential formalism applicable in the entire optical region. J. Opt. Soc. Amer. **72**(7), 839 (1982)
16. Chandezon, J., Maystre, D., Raoult, G.: A new theoretical method for diffraction gratings and its numerical application. J. Opt. **11**(7), 235–241 (1980)
17. Colton, D., Kress, R.: Inverse acoustic and electromagnetic scattering theory, *Applied Mathematical Sciences*, vol. 93, third edn. Springer, New York (2013)
18. COMSOL: COMSOL Multiphysics Reference Manual. COMSOL, Inc., Stockholm, Sweden (2019)
19. Després, B.: Domain decomposition method and the Helmholtz problem. In: Mathematical and numerical aspects of wave propagation phenomena (Strasbourg, 1991), pp. 44–52. SIAM, Philadelphia, PA (1991)
20. Després, B.: Méthodes de décomposition de domaine pour les problèmes de propagation d'ondes en régime harmonique. Le théorème de Borg pour l'équation de Hill vectorielle. Institut National de Recherche en Informatique et en Automatique (INRIA), Rocquencourt (1991). Thèse, Université de Paris IX (Dauphine), Paris, 1991
21. Deville, M.O., Fischer, P.F., Mund, E.H.: High-order methods for incompressible fluid flow, *Cambridge Monographs on Applied and Computational Mathematics*, vol. 9. Cambridge University Press, Cambridge (2002)
22. Ebbesen, T.W., Lezec, H.J., Ghaemi, H.F., Thio, T., Wolff, P.A.: Extraordinary optical transmission through sub-wavelength hole arrays. Nature **391**(6668), 667–669 (1998)
23. Enoch, S., Bonod, N.: Plasmonics: From Basics to Advanced Topics. Springer Series in Optical Sciences. Springer, New York (2012)
24. Godrèche, C. (ed.): Solids far from equilibrium. Cambridge University Press, Cambridge (1992)

25. Gottlieb, D., Orszag, S.A.: Numerical analysis of spectral methods: theory and applications. Society for Industrial and Applied Mathematics, Philadelphia, Pa. (1977). CBMS-NSF Regional Conference Series in Applied Mathematics, No. 26
26. Hesthaven, J.S., Warburton, T.: Nodal discontinuous Galerkin methods, *Texts in Applied Mathematics*, vol. 54. Springer, New York (2008). Algorithms, analysis, and applications
27. Homola, J.: Surface plasmon resonance sensors for detection of chemical and biological species. Chemical Reviews **108**(2), 462–493 (2008)
28. Hong, Y., Nicholls, D.P.: A high–order perturbation of surfaces method for vector electromagnetic scattering by doubly layered periodic crossed gratings. J. Comput. Phys. **372**, 748–772 (2018)
29. Im, H., Lee, S.H., Wittenberg, N.J., Johnson, T.W., Lindquist, N.C., Nagpal, P., Norris, D.J., Oh, S.H.: Template-stripped smooth Ag nanohole arrays with silica shells for surface plasmon resonance biosensing. ACS Nano **5**, 6244–6253 (2011)
30. Johnson, C.: Numerical solution of partial differential equations by the finite element method. Cambridge University Press, Cambridge (1987)
31. Johnson, P., Christy, R.: Optical constants of the noble metals. Physical Review B **6**, 4370 (1972)
32. Jose, J., Jordan, L.R., Johnson, T.W., Lee, S.H., Wittenberg, N.J., Oh, S.H.: Topographically flat substrates with embedded nanoplasmonic devices for biosensing. Adv Funct Mater **23**, 2812–2820 (2013)
33. Kehoe, M., Nicholls, D.P.: Joint geometry/frequency analyticity of fields scattered by periodic layered media. SIAM Journal on Mathematical Analysis (submitted) (2022)
34. Kirsch, A.: Diffraction by periodic structures. In: Inverse problems in mathematical physics (Saariselkä, 1992), *Lecture Notes in Phys.*, vol. 422, pp. 87–102. Springer, Berlin (1993)
35. Kress, R.: Linear integral equations, third edn. Springer-Verlag, New York (2014)
36. LeVeque, R.J.: Finite difference methods for ordinary and partial differential equations. Society for Industrial and Applied Mathematics (SIAM), Philadelphia, PA (2007). Steady-state and time-dependent problems
37. Lions, P.L.: On the Schwarz alternating method. III. A variant for nonoverlapping subdomains. In: Third International Symposium on Domain Decomposition Methods for Partial Differential Equations (Houston, TX, 1989), pp. 202–223. SIAM, Philadelphia, PA (1990)
38. Maier, S.A.: Plasmonics: Fundamentals and Applications. Springer, New York (2007)
39. Moskovits, M.: Surface–enhanced spectroscopy. Reviews of Modern Physics **57**(3), 783–826 (1985)
40. Nagpal, P., Lindquist, N.C., Oh, S.H., Norris, D.J.: Ultrasmooth patterned metals for plasmonics and metamaterials. Science **325**, 594–597 (2009)
41. Natterer, F., Wübbeling, F.: Mathematical methods in image reconstruction. SIAM Monographs on Mathematical Modeling and Computation. Society for Industrial and Applied Mathematics (SIAM), Philadelphia, PA (2001)
42. Nicholls, D.P.: Three–dimensional acoustic scattering by layered media: A novel surface formulation with operator expansions implementation. Proceedings of the Royal Society of London, A **468**, 731–758 (2012)
43. Nicholls, D.P.: Numerical solution of diffraction problems: A high–order perturbation of surfaces/asymptotic waveform evaluation method. SIAM Journal on Numerical Analysis **55**(1), 144–167 (2017)
44. Nicholls, D.P.: On analyticity of linear waves scattered by a layered medium. Journal of Differential Equations **263**(8), 5042–5089 (2017)
45. Nicholls, D.P.: Numerical simulation of grating structures incorporating two–dimensional materials: A high–order perturbation of surfaces framework. SIAM Journal on Applied Mathematics **78**(1), 19–44 (2018)
46. Nicholls, D.P., Reitich, F.: A new approach to analyticity of Dirichlet-Neumann operators. Proc. Roy. Soc. Edinburgh Sect. A **131**(6), 1411–1433 (2001)
47. Nicholls, D.P., Reitich, F.: Stability of high-order perturbative methods for the computation of Dirichlet-Neumann operators. J. Comput. Phys. **170**(1), 276–298 (2001)
48. Nicholls, D.P., Reitich, F.: Analytic continuation of Dirichlet-Neumann operators. Numer. Math. **94**(1), 107–146 (2003)

49. Nicholls, D.P., Reitich, F.: Shape deformations in rough surface scattering: Cancellations, conditioning, and convergence. J. Opt. Soc. Am. A **21**(4), 590–605 (2004)
50. Nicholls, D.P., Reitich, F.: Shape deformations in rough surface scattering: Improved algorithms. J. Opt. Soc. Am. A **21**(4), 606–621 (2004)
51. Nicholls, D.P., Taber, M.: Joint analyticity and analytic continuation for Dirichlet–Neumann operators on doubly perturbed domains. J. Math. Fluid Mech. **10**(2), 238–271 (2008)
52. Petit, R. (ed.): Electromagnetic theory of gratings. Springer-Verlag, Berlin (1980)
53. Phillips, N.A.: A coordinate system having some special advantages for numerical forecasting. Journal of the Atmospheric Sciences **14**(2), 184–185 (1957)
54. Raether, H.: Surface plasmons on smooth and rough surfaces and on gratings. Springer, Berlin (1988)
55. Roache, P.J.: Code verification by the method of manufactured solutions. J. Fluids Eng. **124**(1), 4–10 (2002)
56. Roy, C.J.: Review of code and solution verification procedures for computational simulation. J. Comp. Phys. **205**(1), 131–156 (2005)
57. Sauter, S.A., Schwab, C.: Boundary element methods, *Springer Series in Computational Mathematics*, vol. 39. Springer-Verlag, Berlin (2011). Translated and expanded from the 2004 German original
58. Shen, J., Tang, T.: Spectral and high-order methods with applications, *Mathematics Monograph Series*, vol. 3. Science Press Beijing, Beijing (2006)
59. Shen, J., Tang, T., Wang, L.L.: Spectral methods, *Springer Series in Computational Mathematics*, vol. 41. Springer, Heidelberg (2011). Algorithms, analysis and applications
60. Virieux, J., Operto, S.: An overview of full-waveform inversion in exploration geophysics. Geophysics **74**(6), WCC1–WCC26 (2009)